With theory more easily than experiment, the structural implications of differing multiplicities of the metal atom can be demonstrated. By the changing of the metal d-orbital populations the bond distances in the coordination sphere adjust as would be expected from simple electrostatic arguments.

Although different in derivation, the spectroscopic theory and the theory developed for geometry demonstrate an underlying consistency as demonstrated here, for example, in very similar predictions of spin-state energies. The pattern of orbital energies has been examined in some detail here, and the dependence of the location of the d_{z^2} orbital energy on the strength of the axial ligands relative to the other ligands is discussed. The generally "assumed" splitting of PBP complexes is two sets of degenerate orbitals lower in energy than the axial orbital. The calculations suggest that this ordering can be changed if the axial ligands are weak field, as here, dropping the axial orbital between the two sets of degenerate orbitals.

In summary, $[Fe(DAPSC)(H_2O)_2]^{2+}$ is ideal as a starting point for the further theoretical and experimental study of PBP complexes, and this is actively being pursued.

Acknowledgment. This work was supported in part through a grant from the Office of Naval Research. J.D.B. is grateful for an Eastman Kodak predoctoral fellowship.

Contribution from the Institut für Technische Elektrochemie, Technische Universität Wien, Getreidemarkt 9/158, A-1060 Vienna, Austria

Chemical Bonding in Rutile-Type Compounds

Peter I. Sorantin and Karlheinz Schwarz*

Received May 22, 1991

We present an ab initio study of the bonding in the rutile (TiO_2) structure, where the five members TiO_2, VO_2, CrO_2, RuO_2, and ZnF_2 are investigated by means of band structure calculations, from which we derive electron densities, densities of states, total energies, and structure factors. We present simple molecular orbital schemes in order to interpret the main features of the calculated densities of states. Our results show that a MX_6 cluster model (with M = Ti, Zn, V, Cr, or Ru and X = O or F) accounts only for part of the bonding mechanism. In the crystalline environment, the anionic ligands reduce their amount of π-bonding in the MX_6 cluster at the expense of an increased σ-bonding with all three nearest metal neighbors in the M_3X units. This reduction of anionic π-bonding character causes an increase in the metal–metal bonding across the shared edges of MX_6 octahedra. The observed lattice geometry can be seen as the optimum balance between a maximal stabilization of the MX_6 and the M_3X units. In addition, we determine for one example, namely TiO_2, the internal coordinate u by minimizing the corresponding total energy and obtain a theoretical u of 0.3064 in excellent agreement with the experimental value of 0.305, thus demonstrating the high accuracy of our approach. All calculations are carried out using the full-potential *l*inearized *a*ugmented *p*lane *w*ave (LAPW) method where exchange and correlation effects are treated by the local-density approximation.

1. Introduction

Our interest in the rutile structure type (named after the transition metal (IV)oxide, TiO_2) is motivated by the following four facts: (i) the rutile type is the simplest and most common MX_2 structure where metal atoms M are octahedrally coordinated by ligands X; (ii) in spite of the importance of the rutile structure, we have found only very few theoretical papers most of which are old and do not meet the requirements of modern solid-state chemistry; (iii) the properties of this class of compounds vary wildly from insulating to magnetic and metallic behavior, a variation which is a challenge to theorists; (iv) the rutile type is a demanding test case for applying our procedure of calculating electric field gradients at various atomic sites.

A few additional remarks concerning each of these points are appropriate: Despite the frequent occurrence of this structure type, relatively few related theoretical investigations are found in the literature. The rutile structure is adopted by the transition-metal (IV)oxides and (II)fluorides (3d) TiO_2, VO_2, VF_2, CrO_2, MnO_2, MnF_2, FeF_2, CoF_2, NiF_2, ZnF_2, (4d) RuO_2, PdF_2, and (5d) TaO_2, OsO_2, IrO_2, by the main-group (IV)oxides SiO_2, GeO_2, SnO_2, PbO_2, and by MgF_2. Although structural data are readily available for all of these compounds,[1-7] this has not stimulated much theoretical work with the exception of papers by Baur,[1,2] Goodenough,[8] Caruthers et al.,[9,10] Mattheiss,[11] Gupta et al.,[12] Burdett,[13] Schwarz,[14] Xu et al.,[15] and Glassford et al.[16] Perhaps theorists have been discouraged by the ingenuity of Goodenough's review article[8] on metallic oxides written in 1971. He presented energy diagrams for the common (di)oxide structures to explain the (metallic) behavior of their representatives. His instructive confrontation between experimental data and energy diagrams has substantially influenced work in that field and many interpretations including the present one. However, Goodenough's approach in understanding the properties and bonding in the rutile structure differs significantly from ours; while he built a *phenomenological* model (he calls the chapter on the energy diagrams "Phenomenology") derived from experimental results, our approach is completely *ab initio*. Naturally, there should be a close correspondence between his and our results, and if that is the case,

(1) Baur, W. H. *Acta Crystallogr.* **1976**, *B32*, 2200.
(2) Baur, W. H.; Khan, A. A. *Acta Crystallogr.* **1971**, *B27*, 2133.
(3) Baur, W. H. *Acta Crystallogr.* **1961**, *14*, 209.
(4) Rogers, D. B.; Shannon, R. D.; Sleight, A. W.; Gillson, J. L. *Inorg. Chem.* **1969**, *8*, 841.
(5) Restori, R.; Schwarzenbach, D.; Schneider, J. R. *Acta Crystallogr.* **1987**, *B43*, 251.
(6) Gonschorek, W. *Z. Kristallogr.* **1982**, *160*, 187.
(7) Gonschorek, W. *Z. Kristallogr.* **1982**, *161*, 1.
(8) Goodenough, J. B. *Prog. Solid State Chem.* **1971**, *5*, 145.
(9) Caruthers, E.; Kleinman, L.; Zhang, H. I. *Phys. Rev.* **1972**, *B7*, 3753.
(10) Caruthers, E.; Kleinman, L. *Phys. Rev.* **1972**, *B7*, 3760.
(11) Mattheiss, L. F. *Phys. Rev.* **1976**, *B13*, 2433.
(12) Gupta, M.; Freeman, A. J.; Ellis, D. E. *Phys. Rev.* **1977**, *B16*, 3338.
(13) Burdett, J. K. *Inorg. Chem.* **1985**, *24*, 2244.
(14) Schwarz, K. *J. Phys.* **1986**, *F16*, L211.
(15) Xu, J. H.; Jarlborg, T.; Freeman, A. J. *Phys. Rev.* **1989**, *B40*, 7939.
(16) Glassford, K. M.; Troullier, N.; Martins, J. L.; Chelikowsky, J. R. *Solid State Commun.* **1990**, *76*, 635.
(17) Westman, S. *Acta Chem. Scand.* **1961**, *15*, 217.
(18) Porta, P.; Marezio, M.; Remeika, J. P.; Dernier, P. D. *Mater. Res. Bull.* **1972**, *7*, 157.
(19) Boman, C. E. *Acta Chem. Scand.* **1970**, *24*, 116.

0020-1669/92/1331-0567$03.00/0

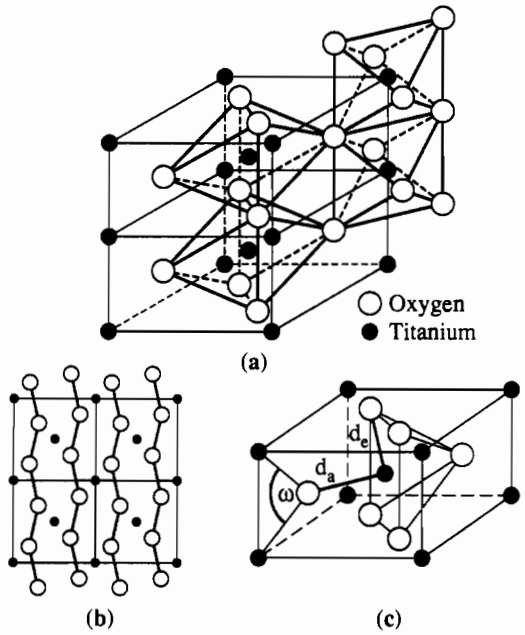

Figure 1. The rutile lattice: (a) coordination polyhedra of the titanium atoms at (0, 0, 0) and ($^1/_2$, $^1/_2$, $^1/_2$); (b) top view of the rutile lattice, the bold lines indicating the almost-hcp planes formed by the oxygen atoms; (c) the two different Ti–O distances d_a and d_e and the bond angle ω.

it demonstrates the chemical significance of our work.

In addition to the chemical bonding presented in this paper, we have calculated the electric field gradient (EFG) tensor at the atomic sites of all compounds. The origin of the EFG and its relationship to the bonding mechanism will be presented in a forthcoming publication.

The present paper is organized as follows: in the next section we will give a short description of the rutile structure, followed by a section "Method" with an overview of our approach to solve Schrödinger's equation by means of the full-potential *l*inearized *a*ugmented *p*lane *w*ave (LAPW) method. In the section "Bonding Mechanism" we present an interpretation of the chemical bonding based on the calculated densities of states, while in the section "Lattice Geometry" we concentrate on the understanding and prediction of the lattice parameters. Finally, we compare our ab initio results with experimental data and other calculations. All computational details are summarized in the Appendix.

2. The Rutile Structure

The rutile structure (Figure 1) is tetragonal with the basis consisting of metal atoms (0, 0, 0) and ($^1/_2$, $^1/_2$, $^1/_2$) and anions located at ($1 \pm u$, $1 \pm u$, 0) and ($^1/_2 \pm u$, $^1/_2 \mp u$, $^1/_2$) with a typical value of 0.3 for the internal coordinate u. Rutile belongs to the nonsymmorphic space group $P4_2/mnm$ (D_{4h}^{14}) in which the metal positions are transformed into each other by a rotation of 90° around the crystal c axis followed by the nonprimitive translation ($^1/_2$, $^1/_2$, $^1/_2$). The two metal positions at the center and the corner of the unit cell are equivalent, when the surrounding octahedra are properly rotated. This symmetry operation can be clearly seen in Figure 1a by looking at the different orientations of the coordination octahedra centered at the two metal positions (0, 0, 0) and ($^1/_2$, $^1/_2$, $^1/_2$).

The rutile structure can also be described by considering an array of anions of approximately hexagonal close-packed (hcp) form (cf. Figure 1b) in which only half of the octahedral holes are occupied by metal atoms.[13] This three-dimensional packing is in contrast to the layered structure found in the related cadmium(II) iodide CdI_2 type. The half-occupation of the octahedral holes, however, leads to a low packing fraction, so that not more than 36% of the unit cell volume can be filled with touching hard spheres. This is caused by the short anion–anion distance between the positions (u, u, 0) and ($1 - u$, $1 - u$, 0). An extreme case is found, for example, in rutile-type SiO_2 (stishovite) where the O–O distance is as short as 2.29 Å, which should be seen in relation to the O^{2-} ionic radius of 1.40 Å. The structure parameters used in this work are summarized in Table I. The metal atoms are octahedrally coordinated by anions which, however, do not form an *ideal* octahedron. The distortion depends on the structure parameters a, c/a, and u and results in two different metal–anion distances shown in Figure 1c. The apical distance d_a is defined between the metal atom at ($^1/_2$, $^1/_2$, $^1/_2$) and the two anions at ($^1/_2 \pm u$, $^1/_2 \mp u$, $^1/_2$), while the equatorial distance d_e is to the four anions at ($1 \pm u$, $1 \pm u$, 0) and ($1 \pm u$, $1 \pm u$, 1). Thus, the distances d_a and d_e represent the height (z axis) and the basal spacing of the "octahedron", respectively, and are given by

Table I. Lattice Constant a, c/a Ratio, Internal Coordinate u, Metal–Anion Distances d_a and d_e, and References Used

	TiO_2	VO_2	CrO_2	RuO_2	ZnF_2
a, Å	4.593	4.530	4.419	4.492	4.704
c/a,	0.644	0.633	0.660	0.692	0.666
u	0.305	0.305	0.303	0.306	0.3024
d_a, Å	1.982	1.954	1.891	1.944	2.013
d_e, Å	1.948	1.901	1.910	1.983	2.045
ref	5	17	18	19	2

$$d_a = \sqrt{2}ua \tag{1}$$

$$d_e = \sqrt{2\left(\frac{1}{2} - u\right)^2 a^2 + \left(\frac{c}{2}\right)^2} \tag{2}$$

These distances d_a and d_e differ by a few percent due to bonding effects (cf. Table I). In the present paper, we will reproduce this variation in distance from our ab initio calculations, where theorists up to now have failed to do so successfully.

For a certain value u^* the two distances d_a and d_e become equal:

$$u = u^* = \frac{1}{4}\left[1 + \frac{1}{2}\left(\frac{c}{a}\right)^2\right] \tag{3}$$

By using this u^* and choosing c/a to make the base plane of the "octahedron" quadratic, one obtains *ideal* octahedral coordination:

$$d_a = d_e \qquad c = \sqrt{2}(1 - 2u)a$$

$$u_{ideal} = \frac{1}{2}(2 - \sqrt{2}) = 0.293 \tag{4}$$

$$(c/a)_{ideal} = 2 - \sqrt{2} = 0.586 \tag{5}$$

Although the actual coordination of the metal atoms deviates from the ideal octahedron, we still call it *octahedral*.

The bond angle ω of the M_3X unit (cf. Figure 1c) is another parameter we will use to characterize the observed lattice geometries and is defined as the angle between the metal atom at (1, 0, 0), the anion at ($^1/_2 + u$, $^1/_2 - u$, $^1/_2$), and the metal atom at (1, 0, 1).

3. Method of Computation

Within the framework of band theory we have used the *l*inear *a*ugmented *p*lane *w*ave method (LAPW) to solve Schrödinger's equation. In the LAPW method[20,21] the unit cell is divided into two types of regions, the atomic spheres centered upon nuclear sites and the interstitial region between the nonoverlapping spheres. The wave function of a Bloch state is expanded in *p*lane *w*aves, but this flexible basis set is used only in the interstitial region, while inside the atomic spheres it is replaced (*a*ugmented) by a much faster converging expansion using atomic-like functions. This dual representation of the wave functions combines the flexibility of a plane wave basis set with the efficiency of an atomic orbital expansion and thus guarantees good convergence. Since we use this augmentation of the plane wave basis, there is no need to introduce

(20) The LAPW method has been introduced by Marcus and Andersen: Marcus, P. M. *Int. J. Quantum Chem., Symp.* **1967**, *1*, 567. Andersen, O. K. *Solid State Commun.* **1973**, *13*, 133.

(21) A theoretical and computational description of our LAPW implementation has been published: Blaha, P.; Schwarz, K.; Sorantin, P. I.; Trickey, S. B. *Comput. Phys. Commun.* **1990**, *59*, 399. The FORTRAN77 code is obtainable from the CPC Program Library.

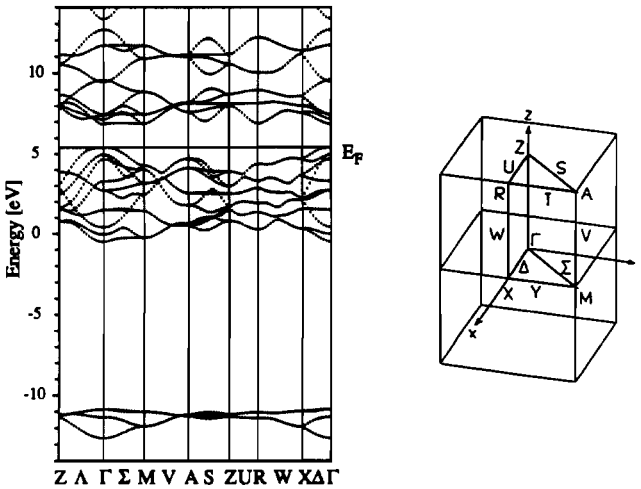

Figure 2. LAPW energy band structure of TiO_2 and corresponding Brillouin zone.

pseudopotentials which lead to smoother wave functions.

The crystal potential (and analogously the charge density) is expanded as

$$V(\vec{r}) = \begin{cases} \sum_{LM} V_{LM}(r) Y_{LM}(\hat{r}) & \vec{r} \in \text{sphere} \\ \sum_{\vec{K}} V(\vec{K}) e^{i\vec{K}\vec{r}} & \vec{r} \in \text{interstitial} \end{cases} \quad (6)$$

where inside the sphere atomic-like functions (radial functions $V_{LM}(r)$ times spherical harmonics $Y_{LM}(\hat{r})$) are used, while a Fourier representation describes the potential in the interstitial region (with $\vec{K}$ being a reciprocal lattice vector). Older implementations of the APW or LAPW scheme have terminated the expansion (6) after the $L = 0$ and $\vec{K} = \vec{0}$ terms, so that the potential (density) was of "muffin-tin" form (spherical average inside the sphere and constant outside). This approximation neglects all nonspherical contributions to the potential and is only tolerable in close-packed structures, but certainly not for rutile-type compounds. We, however, use the fully expanded potential representation (eq 6), commonly called "full-potential", which is obtained from the charge density by solving Poisson's equation.[22] The wave functions in turn are calculated by the LAPW method for a given potential and yield, by summing their squares over the occupied states, the charge density again. This iterative process is repeated till energy eigenvalues and the total energy of two consecutive iterations agree within 0.1 mRy and other convergence criteria (partial charges, electric field gradients) are stable at least to within 1%, so that "self-consistency" is achieved. This procedure makes the results independent of the starting values for ionicities and potentials. Today, self-consistency treatment and the use of a full potential are known to be essential for an accurate band structure calculation. None of the theoretical work mentioned in the Introduction met all these requirements.

In spite of the computational considerations mentioned above, there is at least one fundamental approximation we cannot avoid making even in the full-potential LAPW code. This is the reduction of the many-body problem we have to solve to an effective one-particle formalism by the local-density approximation (LDA). The LDA allows us to describe the nonclassical effects of exchange and correlation but restricts investigations to ground-state properties. This is not a severe restriction for the present study, in which we are mainly interested in charge densities, lattice geometries, and structure factors. The LAPW method is among the most accurate schemes to obtain results within the LDA framework.

4. Bonding Mechanism

Each of the five compounds we have investigated has special chemical and physical properties: (i) We have chosen rutile TiO_2 because it is insulating and the archetype of the structure. (ii) Rutile-type VO_2 exists only above 341 K and is a poor metal; at 341 K it undergoes a phase transition to a monoclinic, semiconducting modification. (iii) CrO_2 is a ferromagnetic metal; earlier studies (Schwarz[14]) predicted CrO_2 to be a "half-metallic ferromagnet", which means it is metallic for spin-up but semiconducting for spin-down electrons. (iv) RuO_2 has been chosen as typical metallic compound of the 4d series. (v) ZnF_2, an insulator, has been selected to investigate a (II)fluoride and a closed d-shell system.

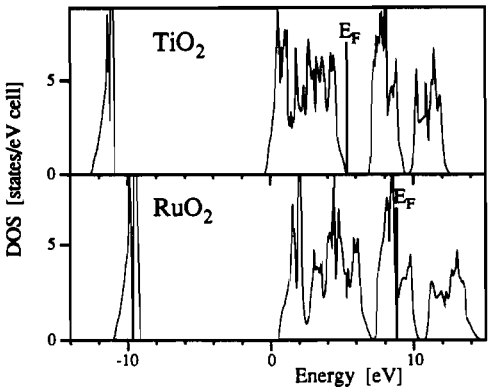

Figure 3. Density of states (DOS) for TiO_2 and RuO_2.

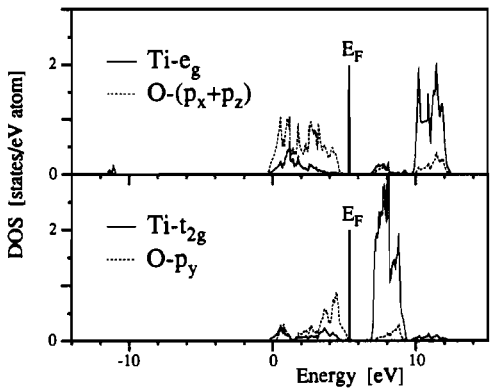

Figure 4. Decomposition of the TiO_2 density of states (DOS). The DOS is decomposed into Ti e_g, O $p_x + p_z$, and Ti t_{2g} + O p_y contributions, which are normalized to one atom.

4.1. Band Structure and Density of States. The basis of our interpretation is the density of states (DOS) from which we will draw conclusions about the orbital interactions between the atoms. These interactions will be characterized in the form of molecular orbital diagrams (MO diagrams). We will use these illustrations intensively in our discussion, because they transfer the discussion from the reciprocal space of band structure to the "more chemical" direct space of the crystal lattice.

Figure 2 shows the energy bands of TiO_2 with three groups of bands: (i) the low-lying states around −12 eV coming from the oxygen 2s orbitals, (ii) the bands between 0 and 5 eV originating mainly from oxygen 2p orbitals, and (iii) the bands above the Fermi energy dominated by contributions from titanium 3d orbitals. The corresponding densities of states for all four (IV)oxides studied here are rather similar. As an example the DOS's for TiO_2 and RuO_2 are shown in Figure 3. The similarity in the DOS's is a strong indication that the (IV)oxides follow analogous bonding mechanisms despite their very different properties (the quite different DOS of ZnF_2 in Figure 9 will be discussed later). We have chosen the TiO_2 DOS for the detailed investigation below, but the other (IV)oxide DOS's would give similar results.

The decomposition of the total TiO_2 DOS into contributions from the metal d and ligand p orbitals gives further information about orbital partnerships in the bond formation (see Figure 4).

The σ- and π-bonds require proper spatial orientation of the involved atomic orbitals. We make this obvious statement explicitly, since the coordinate systems, in which the p and d orbitals are defined, are nontrivially oriented with respect to the crystal axes. The coordinate systems of titanium and oxygen do not coincide, and both differ from that of the global crystal (unit cell). Inside the titanium sphere we have chosen the orientation typical for ligand field theory where the axes point from the central atom

(22) Weinert, M. *J. Math. Phys.* **1981**, *22*, 2433.

to the six ligands, while at the oxygen site only the z axis (in the negative direction) is directed toward a titanium neighbor. Both "local" coordinate systems are shown in Figure 13 of the Appendix.

The TiO_2 DOS (Figures 3 and 4) is clearly separated into four main peaks which are labeled according to their predominant l character as mentioned above in the description of the band structure: (i) the oxygen "s states" around −11 eV; (ii) the oxygen "p states" below E_F; (iii) the titanium "t_{2g} states" centered at 8 eV; (iv) the titanium "e_g states" at 11 eV. The Fermi energy falls in the direct gap between the oxygen p and titanium t_{2g} states.

4.2. MO Diagrams. The splitting of metal d states in a t_{2g} and e_g region is to be expected in an octahedral ligand field. We have shown above ("Structure" section) that the octahedron in the rutile structure is not perfect, since u and c/a differ from the ideal values of eqs 4 and 5. Nevertheless, it is more convenient to label the DOS according to the well-known symmetry classification of t_{2g}/e_g rather than to the (lower) actual point group symmetry. The titanium DOS above the Fermi energy shows that the classification according to these two symmetries is justified, since the t_{2g} DOS contains only a small admixture from the e_g symmetry and vice versa; furthermore, the broadening influence by the oxygen interaction is small. The mixing between titanium and oxygen orbitals gives us some insight into the bond formation: the t_{2g} states indicate strong interactions with the oxygen p_y states, while the p_x and p_z states dominate in the e_g region.

The interpretation is made much easier by considering hybridization: In the rutile structure the oxygen atoms are surrounded by three metal atoms, yielding a M_3X cluster. This M_3X cluster has a perfectly planar geometry with two identical bond angles of about 130° and one angle of about 100° (called ω; cf. Figure 1c). Geometries like this call for an sp^2 hybridization of the central X atom to form three σ-bonds (from p_x and p_z) in the plane and *one* π-bond (from p_y) perpendicular to the plane.

For the metal atom the following hybrids are useful: (i) The metal e_g orbitals are combined with s and p functions to form six hybrid orbitals $e_g^2sp^3$ pointing toward the ligands, so that σ-bonding with ligand sp^2 orbitals is expected. (ii) From the three t_{2g} orbitals, two, namely d_{xz} and d_{yz} (Figure 13), are added and subtracted to yield one hybrid orbital (d_{xz+yz}) perpendicular and one (d_{xz-yz}) parallel to the [001] plane; the latter has a node in the base plane of the octahedron and is properly oriented to yield a π-bond with the p_y orbital of the apical oxygen; the other combination (d_{xy+yz}) lies in the [110] plane and could lead to a π-bond with the p_x orbital of the apical oxygen, but this bond turns out to be weak. This comes about since the oxygen p_x orbitals are mainly engaged in σ-bonds with the e_g hybrids. The ligands of an octahedral MX_6 cluster normally are involved in two π-bonds (p_x, p_y) and *one* σ-bond (p_z), while, in the rutile type solids or a M_3X cluster, the formation of one π-bond (from ligand p_y and metal t_{2g}) and *two* σ-bonds (from ligand p_x and p_z and metal $e_g^2sp^3$) is preferred. This surprising result of a reduced ligand π-bonding is caused by the crystal environment of the ligands, where they have three bonding partners. The chemical formulas of the cluster and the unit cell, MX_6 and M_2X_4, respectively, express most easily the different coordination of the anions and the related shortcoming of a simple MX_6 picture. In the solid, it is at least necessary to consider the bonding in the M_3X cluster as well as that in the MX_6 cluster.

The anionic preference of σ-bonding must have effects on the three metal t_{2g} orbitals: only d_{xy+yz} has a π-bonding anionic counterpart, while the d_{xy-yz} and d_{xy} either are nonbonding or interact with the corresponding metal orbitals a lattice vector (0, 0, c) apart. The overlapping d_{xy} and d_{xy-yz} orbitals will give one σ-type and one π-type metal–metal bond along the shared edges of the octahedra. Their bond strengths are expected to be low, because of the large metal–metal distance.

We will now present a molecular orbital scheme for the rutile-type oxides which considers all bonding effects discussed so far (see Figure 5).

We have already split the degenerate atomic d levels of titanium into hybridized t_{2g} and e_g states, which makes Figure 5 more clearly structured. There is evidence from Figure 4 that the oxygen p_y orbitals are partly nonbonding, judged by its DOS, since there

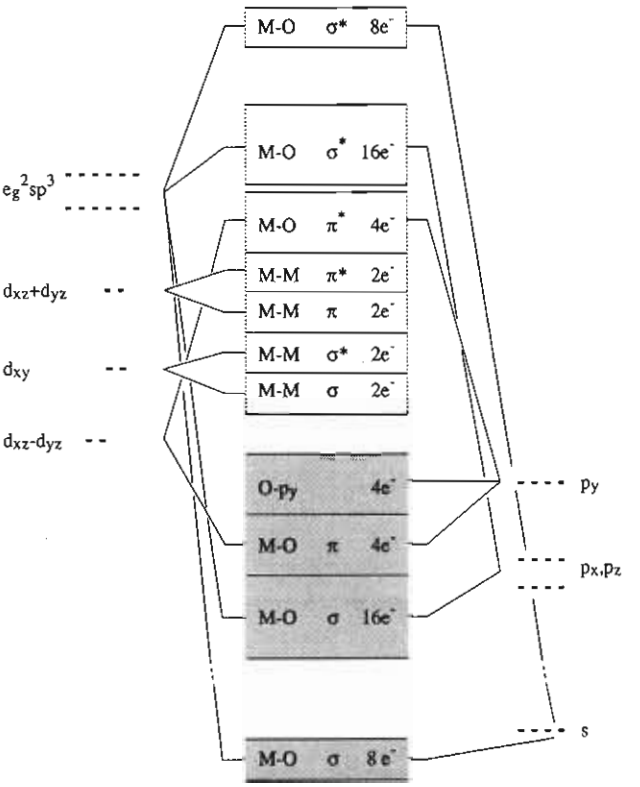

Figure 5. Molecular orbital scheme for a rutile-type (IV)oxide M_2O_4. The energy levels occupied by TiO_2 are represented by gray shadings. The coordination system used for the atoms are shown in Figure 13.

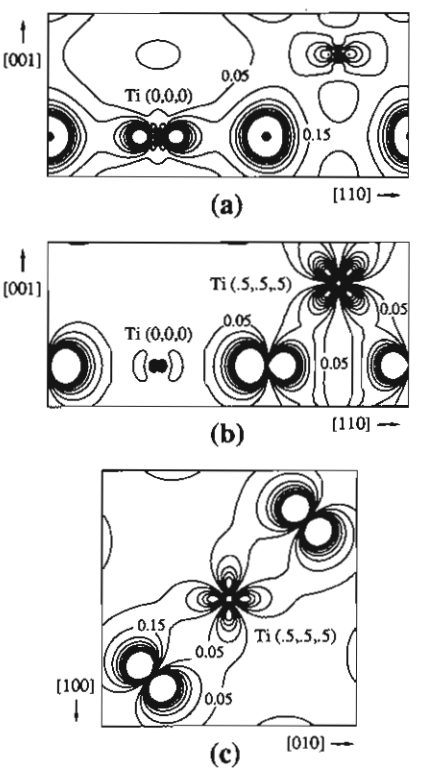

Figure 6. Electron densities of three TiO_2 band states at the $\vec{k}$ point Z (0, 0, π/c) at one boundary of the Brillouin zone: (a) valence-band state no. 5, in the (1$\bar{1}$0) plane; (b) valence-band state no. 11, in the (1$\bar{1}$0) plane; (c) valence-band state no. 13, in the (002) plane. The contour values range from 0.05 to 0.75 e Å^{-3} with an increment of 0.1 e Å^{-3}.

is a sharp peak at the upper edge of the p states. This peak is rather broad in TiO_2 but is sharper in the other (IV)oxides.

The MO scheme of Figure 5 is of course only qualitative and cannot give a full description of the bonding variety in a solid.

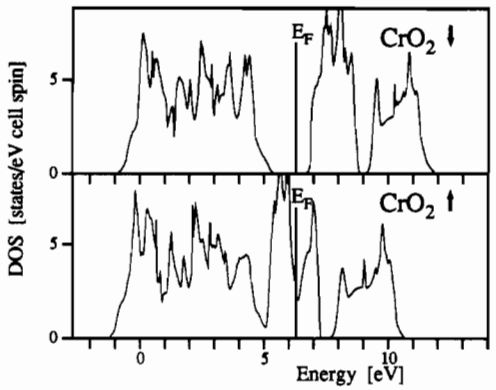

Figure 7. Spin-polarized CrO_2 density of states (DOS). The narrow oxygen s states at −12 eV are not shown.

However, the MO scheme gives a very instructive description of typical DOS features. Additionally, it enables us to classify the DOS according to its bonding, antibonding, or nonbonding character, features which will be used to estimate the lattice geometry of the rutile-type compounds in the following section.

4.3. Electron Densities. The MO scheme is illustrated by showing (Figure 6) the electron densities of selected band states of TiO_2 at the Z point $(0, 0, \pi/c)$ in the Brillouin zone. In this case the mixing between different atomic orbitals is relatively low because of the high symmetry of the Z point, so that bonding interactions can be easily classified.

Parts a and b of Figure 6 correspond to band states from the low-energy region of the p bands and show the axial and equatorial titanium–oxygen σ-bonding just as formulated in the MO scheme. The plot in Figure 6c has been calculated from a band state at the upper edge of the p bands and shows the postulated titanium–oxygen π-interaction. Examples for all other bonding types found in the MO scheme could also be given.

4.4. Fermi Energy Positions. The very different electrical conductivities[4] of the rutile-type oxides are easily explained by the calculated positions of the Fermi energies E_F:

(i) TiO_2 is a very stable compound and is insulating, because the Fermi energy falls in the large gap between the oxygen p and titanium t_{2g} bands. The MO scheme indicates that all occupied states are bonding.

(ii) The Fermi energy of VO_2 lies within the sharp peaks of the t_{2g} states, and therefore VO_2 is metallic. The high DOS value at E_F indicates why tetragonal VO_2 is close to a structural instability leading to a monoclinic modification.

(iii) RuO_2 is a metal with a Fermi energy in the t_{2g} range of the DOS, analogous to VO_2. However, in contrast to VO_2, RuO_2 is a stable compound, since the Fermi energy falls in the relative minimum of the DOS between peaks originating from ruthenium–oxygen π and π^* states (Figure 3).

(iv) Paramagnetic CrO_2 would have a Fermi energy positioned in a peak of the t_{2g} states, as in VO_2. Instead of undergoing a phase transition in order to avoid this high DOS, a highly unstable situation, CrO_2 becomes ferromagnetic with a moment of exactly 2 μ_B.[23] The two cases TiO_2 and RuO_2 show stable configurations where, in the former case, all states up to bands of predominantly oxygen p character are occupied, while, in the latter case, the states of t_{2g} symmetry are filled up to the pronounced minimum occurring in its DOS. We have found that CrO_2 adopts both situations by spin polarization, so that the spin-up DOS (Figure 7) closely resembles that of metallic RuO_2, while the spin-down DOS is comparable to that of insulating TiO_2 (so-called half-metallic ferromagnet).

Spin-up and spin-down states of chromium are shifted by the exchange-splitting against each other till the local minimum of the spin-up t_{2g} DOS falls within the gap of the spin-down DOS between the oxygen p and the chromium t_{2g} states, respectively. The gap in the spin-down DOS around the Fermi energy leads

(23) Kubota, B. *J. Phys. Soc. Jpn.* **1960**, *15*, 1706.

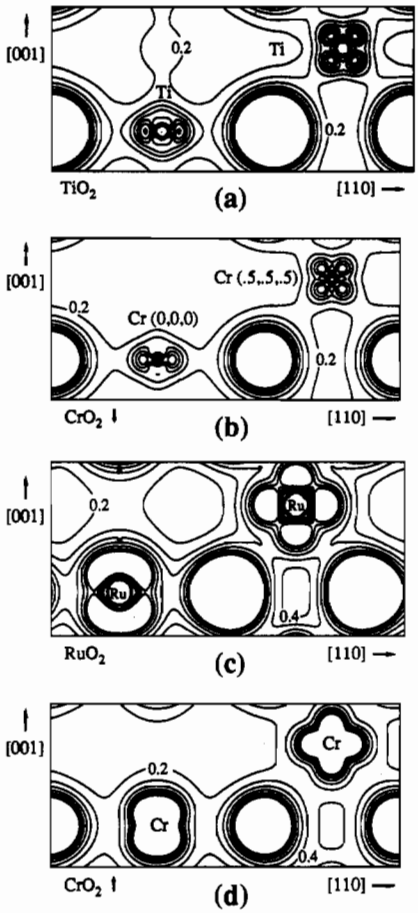

Figure 8. Valence electron densities in the $(1\bar{1}0)$ plane: (a) TiO_2; (b) CrO_2 (spin-down); (c) RuO_2; (d) CrO_2 (spin-up). Contour values range from 0.2 to 1.4 e Å^{-3} with an increment of 0.2 e Å^{-3}.

to 100% spin polarization at E_F, and the fact that the spin-down t_{2g} states remain unoccupied leads to an integer magnetic moment of 2 μ_B. The similarity of the two CrO_2 spin subsystems to those of TiO_2 and RuO_2 is illustrated by Figure 8, where we have plotted the valence electron densities of TiO_2 (Figure 8a) and RuO_2 (Figure 8c), which should be compared to the CrO_2 spin-down (Figure 8b) and spin-up (Figure 8d) density.

Our results confirm the earlier calculations by Schwarz,[14] who predicted that CrO_2 is a "half-metallic ferromagnet". For a comparison with experimental data see section "Comparing Theory with Experiment".

Besides the similarity to CrO_2 discussed above, parts a and c of Figure 8 show a remarkable change in symmetry of the electron densities going from TiO_2 to RuO_2. In TiO_2, the density has mostly pure e_g character, while the valence density of RuO_2 is dominated by t_{2g} symmetry. This change is induced by the additional occupation of t_{2g} states in RuO_2.

4.5. The Fluoride ZnF_2. The present LDA calculation predicts a gap of about 4 eV for zinc(II) fluoride, ZnF_2 (see the discussion of LDA gap values in the section "Comparing Theory with Experiment"—TiO_2). Since this gap is large, the DOS of the unoccupied states is not shown in Figure 9.

The most significant features of the ZnF_2 DOS are illustrated by showing the *l*-decomposed DOS in Figure 9: the zinc t_{2g} states (centered at about −3.5 eV) and the fluorine p_y states (at about −1.4 eV) give rise to sharp peaks in the corresponding DOS, which do not overlap or strongly mix and therefore originate from mostly nonbonding orbitals. This weakening of covalency compared to the (IV)oxides is caused by the much smaller polarizability of F^- with respect to O^{2-} and by the reduced spatial extension of the fluorine orbitals in comparison to those of the oxygen ligands. This higher localization of the fluorine orbitals primarily reduces the π-interaction between zinc and fluorine. Orbitals, which are π-bonding in the (IV)oxides, form essentially nonbonding states

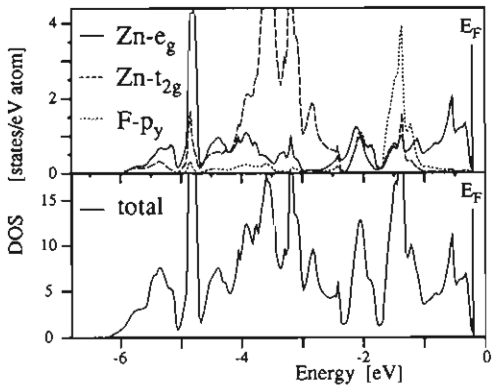

Figure 9. Decomposition of the ZnF_2 density of states (DOS). The total DOS (lower window) is decomposed into Zn $e_g + t_{2g}$ and F p_y contributions (upper window), which are normalized to one atom. The narrow fluorine s states at −21 eV are not shown.

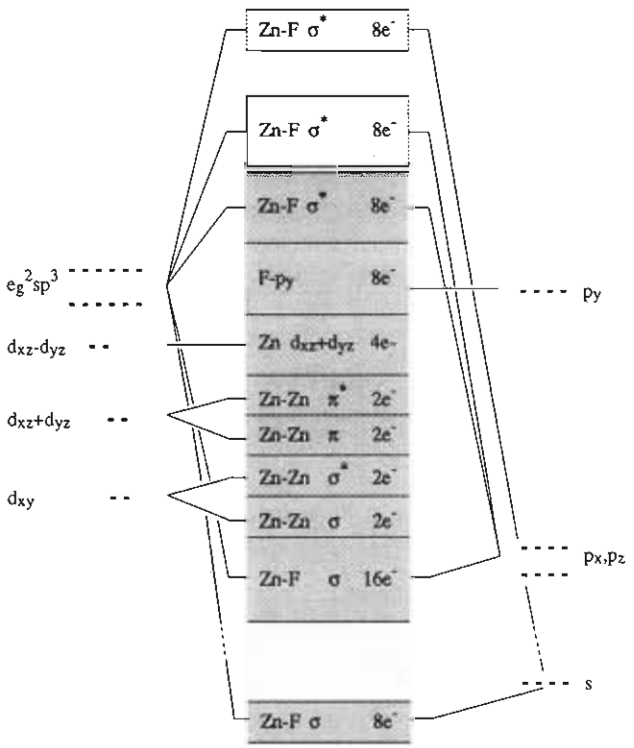

Figure 10. Molecular orbital scheme for zinc(II) fluoride. The energy levels occupied by ZnF_2 are represented by gray shadings. The coordination systems used for the atoms are shown in Figure 13.

in the (II)fluorides. By taking these considerations into account, we can modify the MO scheme of the (IV)oxides to ZnF_2 (see Figure 10).

The fluorine p_y orbitals are fully occupied, since they are essentially nonbonding, as shown in the MO scheme of Figure 10. The p_x and the p_z orbital, however, interact strongly with zinc e_g states, thus giving bonding and antibonding σ states, where the latter are only partly occupied. This situation leads to a much higher p_y charge in comparison to the p symmetries observed in the (IV)oxides. This difference in occupation numbers causes an asphericity in the valence electron density of ZnF_2, which can best be demonstrated by plotting deformation densities with respect to superposed free atoms. The higher occupation of the p_y orbitals can be clearly observed in Figure 11c for ZnF_2, while the p_x and p_z symmetries dominate for TiO_2, as can be seen in Figure 11a,b.

5. Lattice Geometry

As already pointed out, the rutile lattice is completely described by the lattice parameter a, the c/a ratio, and the internal coordinate u. We will refer to these parameters simply as "lattice geometry".

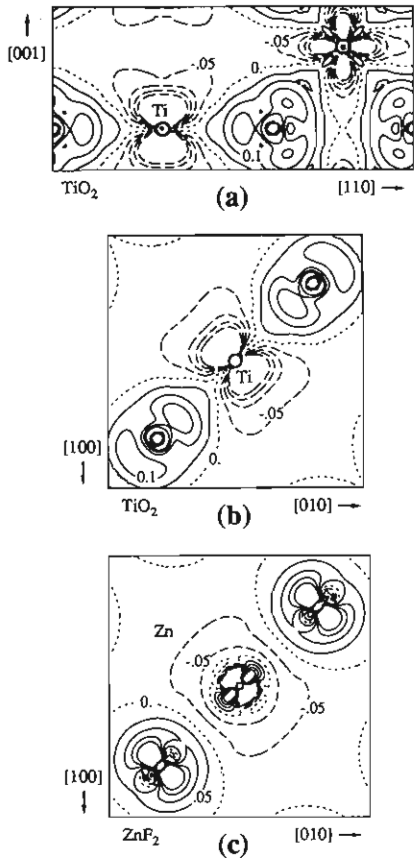

Figure 11. Deformation densities of TiO_2 and ZnF_2. The deformation densities are defined by the LAPW crystal density minus the density of superposed free atoms (Ti $4s^2$, $3d^2$; O $2s^2$, $2p^4$; Zn $4s^2$, $3d^{10}$; F $2s^2$, $2p^5$): (a) TiO_2, in the $(1\bar{1}0)$ plane; (b) TiO_2, in the (002) plane; (c) ZnF_2, in the (002) plane. Dashed contours indicate negative densities, the zero contour is dotted, and full contours represent positive densities; the contour values range from −0.2 to 0.2 e $Å^{-3}$ with an increment of 0.05 e $Å^{-3}$.

So far, several attempts have been made to give an estimate of the lattice geometry of a compound within the rutile family. The simplest but also the most general idea was put forward by O'Keeffe,[24] who suggested that (ionic) crystals tend to maximize the unit cell volume Ω under the constraint of a fixed cation–anion distance. O'Keeffe expressed Ω as a function of u only, which is possible by setting d_a equal to d_c. He then calculated the "maximum-volume structure" of the rutile lattice by maximizing Ω with respect to u. He thus obtained u and c/a values of 0.300 and 0.632, which are both near the observed values. Baur[1] tried to relate a mean metal–anion distance and u to the c/a ratio. However, the only trend he could describe concerns the main-group (IV)oxides, for which the mean metal–anion distance increases with c/a. A more successful approach was that of Rogers et al.,[4] who plotted the c/a ratio of the 3d, 4d, and 5d (IV)oxides against the number of metal d electrons n_d. Their plot shows approximately the same variation with c/a for each d series. At the beginning of a d series, there is always a deep minimum in c/a (at $n_{3d} = 1$, $n_{4d} = 3$, and $n_{5d} = 2$) which is immediately followed by the maximal c/a value (at $n_{3d} = 2$, $n_{4d} = 4$, and $n_{5d} = 4$). Rogers et al. ascribed this trend to the varying occupation of the bonding or antibonding metal–metal states, respectively, as governed by the number of d electrons.

These examples clearly indicate that lattice geometry is not ruled by one effect only. O'Keeffe's principle works quite nicely, because it includes both electrostatics *and* covalency. His procedure reduces the electrostatic anion–anion repulsion by maximizing the unit cell volume but maintains covalent interactions by keeping cation–anion distances fixed. Interpretations based solely on a MO scheme can only partially answer the questions

(24) O'Keeffe, M. *Acta Crystallogr.* **1977**, *A33*, 924.

about lattice geometry, since the influence of electrostatics is completely neglected. We take rutile as an example: all occupied states in the MO scheme of TiO_2 are bonding, suggesting that in this case there should be the shortest metal–oxygen distances d_a and d_e within the 3d (IV)oxides. Since this is not the case, it further underscores the importance of electrostatic repulsions between neighboring anions. Repulsion tends to increase spacing between anions, thereby yielding small u coordinates and an enlarged d_e metal–anion distance. This "electrostatic" effect is most pronounced in TiO_2, where the ionic character is highest within the 3d (IV)oxides.

5.1. Understanding the c/a Ratio and Bond Lengths. Apart from the limitations mentioned above, the MO model remains a useful tool for tracing trends in the properties of the rutile-type compounds. Our density of states corroborates the idea of Marinder[25] and Rogers,[4] namely that changes in the c/a ratios depend on the formation of metal–metal bonds. The following survey discusses these aspects of lattice geometry as related to certain types of occupied states within the MO scheme of Figure 5.

We have already shown that a perfect octahedral symmetry of the TiO_6 units would yield a very unfavorable oxygen coordination in the planar Ti_3O units with bond angles of 90° and twice 135°. An improvement of this anionic coordination toward the preferred bond angles of 120° of the ideal sp^2 symmetry can be achieved by increasing either the c/a or u value over the $(c/a)_{ideal}$ or u_{ideal} value (cf. eqs 5 and 4), however with totally different effects on both Ti–O distances: an increase of c/a enlarges d_e, while an increase of u reduces d_e and enlarges d_a. The lattice geometry is determined by both mechanisms. From the experimentally observed relation $d_a > d_e$, we find that the increase due to u is more important than the increase by c/a. Thus the *two* axial Ti–O σ-bonds inside the octahedra are weakened while the *four* equatorial Ti–O σ-bonds are strengthened.

VO_2 is the first compound in the 3d series where metal–metal bonding occurs. This metal–metal interaction is bonding and leads to a remarkable shortening of the crystal c axis. The corresponding reduction of the c/a ratio makes the relation $d_a > d_e$ even more distinct.

The lattice geometry of CrO_2 is determined by metal–metal bonding as in VO_2, but the higher electron count causes the interaction to become an antibonding and repulsive one. Therefore, the c/a ratio is increased with respect to TiO_2 to the extent that we find for the metal–ligand distances $d_a < d_e$.

Within the 4d series there are enough electrons from RuO_2 upward to exhibit a full occupation of the antibonding metal–metal states, leading to a very high c/a ratio and a d_e distance which is unfavorably large. A reduction of d_e by increasing the u coordinate does not work, since it would enlarge the d_a spacing as well as strengthen the electrostatic repulsion by lowering the oxygen–oxygen distance. In order to avoid this unfavorable effect, the lattice parameter a is decreased to increase the c/a ratio. The a value in RuO_2 is even smaller than that in TiO_2 or VO_2.

In ZnF_2, electrostatics is more important than it is in the (IV)oxides, since covalency is reduced. A small u coordinate allows the lattice geometry to avoid a close contact of the fluorine atoms at the shared edges of the octahedra. The occupied antibonding metal–metal states cause the large c/a ratio.

In spite of the trends discussed so far, we find that the c/a ratio and the u coordinate are not the proper parameters to establish an explicit relationship between chemical bonding and lattice geometry. Both lattice parameters are well suited for a geometrical description of the lattice but cannot be assigned exclusively to certain bonding effects. In the previous section, we showed that the observed lattice geometry is the best compromise optimizing different structure units. The geometrical constraints of these units were noted as follows: (i) approximately equal bond angles in the planar M_3X units; (ii) short metal–anion distance d_a; (iii) short metal–anion distance d_e; (iv) a large ligand–ligand spacing to minimize the electrostatic repulsion along the shared edges of the octahedra; (v) a short crystal c axis to increase metal–metal bonding; (vi) a small rectangular distortion of the octahedral base plane to provide the geometry for a good metal–ligand σ-interaction.

Table II. Influence of Six Lattice Geometry Constraints on the Lattice Parameters a and c, the c/a Ratio, and the Internal Coordinate u[a]

geometry constraint	influence on lattice parameter			
$\omega \rightarrow 120°$			c/a large	u large
M–X: d_a min	a small		c/a large	u small
M–X: d_e min	a small	c small		u large
X–X: max	a large		c/a small	u small
M–M: min		c small	c/a small	
base plane → quadratic	a large	c small	c/a small	

[a] ω is the bond angle shown in Figure 1c; M–X, X–X, and M–M symbolize interatomic distances (where M stands for metal and X stands for ligand atom); the base plane is formed by the anions at $(1 \pm u, 1 \pm u, 0)$ and at $(1 \pm u, 1 \pm u, 1)$.

Table II summarizes the influence of these six effects on the c/a ratio and the internal coordinate u.

In Table II all covalent interactions have been assumed to be attractive. This is a considerable simplification, since antibonding states will be occupied by higher electron counts and formerly attractive interactions will become repulsive ones. Even with this simplification, the variety of competing effects in Table II interdicts conclusions about chemical bonding from the c/a and u values. This is why Baur[1] could not establish a c/a dependency of u and why he could not find chemically related compounds to follow a universal curve.

5.2. Ab Initio Determination of the Internal Coordinate u. In contrast to the MO model, the LAPW method includes all types of interactions in the electronic potential. Minimizing the total energy E_{tot} with respect to a given structural parameter allows us to determine this parameter from first principles, and even quantitatively. This is a clear advantage of the total energy concept over the previous estimates derived from the MO picture. There is, however, the disadvantage that the interpretation is more difficult, since the relation between structural parameters and the various interactions, which are all included in the electronic potential, is no longer explicit but merely implicit.

We have chosen the internal coordinate u of TiO_2 to be determined by a total energy[21,26] minimization, keeping the cell dimensions (a and c) fixed. We have performed a series of five self-consistent calculations for selected u values. The resulting function $E_{tot}(u)$ shown in Figure 12a has been fitted by a quadratic polynomial. From this fit we have analytically derived the energy minimum and the corresponding u value u_{min} of 0.3064.

There is a very satisfying agreement between our calculated u_{min} value of 0.3064 and the experimental value[5] of 0.305.

Up to now two similar attempts to determine u have been made by Burdett[13] and by Glassford et al.[16] Burdett's very interesting paper deals with the overall stability of the rutile structure and its distorted variants. By means of a total energy minimization (applying the extended Hückel method) he has determined a u_{min} value of 0.297 for TiO_2. Deviation from experiment is relatively large, especially considering the sharp rise of his total energy function when deviating from the optimum u value. A population analysis of Burdett's wave functions points to the basic shortcoming of his model: the overlap population corresponding to the short equatorial Ti–O bond is smaller than that of the long axial Ti–O bond, in contrast to expectations. The augmented plane wave basis used in our calculations does not allow us to uniquely determine overlap populations. We have tried to estimate the equatorial and the axial Ti–O *bond charge* by analyzing the partial charges within the titanium sphere. The titanium e_g charge can be decomposed into the two components of d_{z^2} and $d_{x^2-y^2}$ symmetries, which represent approximately the axial and equatorial bond charges. Figure 12b shows how these partial charges and the bond lengths

(25) Marinder, B.-O.; Magneli, A. *Acta Chem. Scand.* **1957**, *11*, 1635.

(26) Weinert, M.; Wimmer, E.; Freeman, A. J. *Phys. Rev.* **1982**, *B26*, 4571.

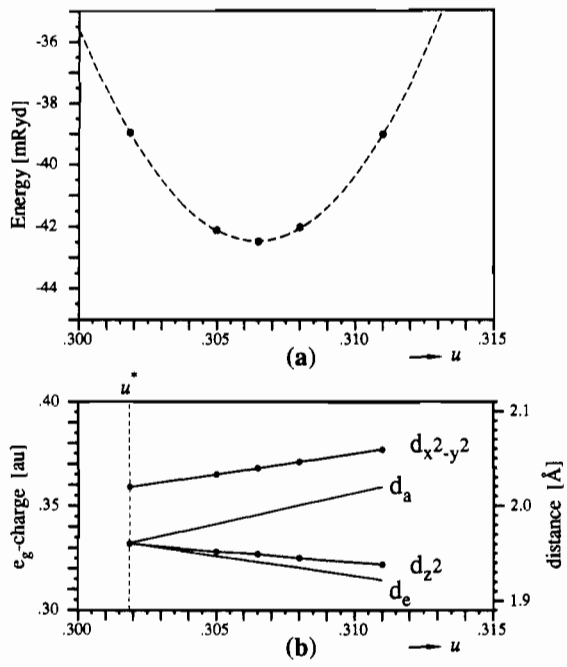

Figure 12. Dependency of TiO_2 properties on the internal coordinate u: (a) total energy of TiO_2 (shifted by +4007.3 Ry) as a function of u (dashed function fitted to the five $E_{tot}(u)$ values marked with circles); (b) titanium e_g charge and Ti–O distances d_a and d_e as functions of u (u^* is the u value to give $d_a = d_e$).

d_a and d_e vary with u: increasing u above u^* causes d_a to rise and d_e to fall, while the related bond charges increase when the corresponding bond length is decreased. For u^* (where $d_a = d_e$) the $d_{x^2-y^2}$ equatorial charge is already greater than the axial one, so that the equatorial bond is favored and will be the shorter in the actual structure.

The ab initio calculations of Glassford et al.[16] are based on the pseudopotential method and the local-density approximation. In the determination of u they follow the general approach of minimizing the total energy. In addition to u, they have calculated the lattice parameters a and c and the bulk modulus and its derivative, as well as the cohesive energy. Glassford et al. have found a u_{min} value of 0.3048, which is in excellent agreement with diffraction measurement,[5,7] while the theoretical lattice parameters a and c are larger than the experimental ones, but by less than 2%. This deviation has been observed in many other calculations, although it is unusual that lattice parameters determined by LDA calculations are *larger* than those found in experiments.

6. Comparing Theory with Experiment

In this section, we compare the results obtained from ab initio calculations with various experimental data. Since we use the local-density approximation, which is only valid for ground-state properties, we are especially interested in experiments providing information about the electronic ground state of a crystal. This type of result can be obtained by X-ray, γ-ray, or neutron diffraction as well as by measuring the electric field gradient. (The latter topic will be published separately in a forthcoming paper.) All other experiments referred to in this section, such as photoelectron spectra or optical reflectivity measurements, involve electronic excitations, which can only be approximately estimated from our ground-state LAPW results.

We will focus our discussion on the archetype TiO_2 and on the probably technologically most interesting compound, CrO_2.

6.1. TiO_2. The lattice parameters and the charge density of TiO_2 have been intensively studied by diffraction experiments. Restori, Schwarzenbach, and Schneider[5] collected highly precise X-ray data sets for three single crystals at 100 and 295 K. They studied very carefully the influence of various data refinement procedures on the resulting static structure factors and deformation maps. To minimize scaling errors in the refined X-ray intensities, they measured five low-order γ-ray structure factors on an absolute scale and thus determined an experimental scale factor. The values of the structural parameters a, c, and u found by Restori et al. are given in Table I; they have been the basis of our TiO_2 calculation. Unfortunately these investigations of Restori et al. indicate a strong influence of the applied refinement procedures on the deformation maps. The only features common to all maps are (i) nearly identical charge maxima of about 0.25–0.3 e Å^{-3} in both Ti–O bonds, where the slightly higher values are located in the longer axial bond d_a, and (ii) a negative deformation density at the Ti sites, directed along the crystal c axis. Figure 11a shows the deformation map generated from the LAPW electron density. In agreement with Restori et al., we find positive charge maxima in both Ti–O bonds and a negative deformation density elongated along the c axis at the Ti sites. However, our charge maxima have a value of about 0.20 e Å^{-3} and occur in the short equatorial Ti–O bond.

Table III. Calculated Low-Index (Static) LAPW Structure Factors of Rutile-Type TiO_2, VO_2, CrO_2 (Spin-Up), CrO_2 (Spin-Down), RuO_2, and ZnF_2 (in Electrons)

hkl	TiO_2	VO_2	$CrO_2\uparrow$	$CrO_2\downarrow$	RuO_2	ZnF_2
110	37.76	39.69	22.20	19.06	77.57	55.06
101	23.61	25.48	15.28	12.60	62.01	39.82
200	13.57	15.51	9.84	7.27	50.77	26.56
111	−18.93	−18.49	−9.19	−9.45	−18.74	−23.27
210	12.23	12.06	5.69	5.74	12.11	14.30
211	30.67	31.90	17.42	15.92	64.25	47.70
220	35.33	36.46	19.76	18.34	67.48	53.85
002	38.70	39.31	21.24	20.15	72.95	59.12
301	34.33	35.25	18.47	17.52	65.15	51.73
400	22.28	23.25	12.76	12.02	50.50	36.67
330	27.10	27.80	14.36	13.79	54.80	40.81
004	21.85	21.99	11.50	11.40	46.63	31.72

Another data set of TiO_2 X-ray intensities was collected by Gonschorek.[6] He investigated four rutile single crystals at room temperature on an absolute scale. The analysis of his electron density shows maxima for the short equatorial Ti–O bonds in agreement with our deformation map, but the axial bond does not show a relative maximum at all. In a neutron diffraction study Gonschorek[7] determined the internal coordinate u of TiO_2 and found a value of 0.3048, in very good agreement with the result of Restori et al.

The bonding mechanism presented above gives no reason for a higher electronic charge at the longer bond distance. Therefore, we believe our results to be closer to reality than that of Restori et al. Table III lists selected static structure factors of TiO_2 and the other compounds, calculated as the Fourier transform of the LAPW charge density.

Since the static structure factors of Restori et al. depend so strongly on the refinement model used, we did not compare our results in Table III with one of the refined experimental data sets.

Kowalczyk et al.[27] studied the valence-band DOS of insulating oxides by X-ray photoelectron spectroscopy (XPS). In the case of TiO_2, he found a valence bandwidth of 5.4 eV. In the terminology of this paper Kowalczyk's valence bands are called the anionic p bands and they have a width of about 5.7 eV (Figures 3 and 4). Kowalczyk reported an energy separation of 1.9 eV between "the two major features in the valence band". We cannot locate such a double-peak structure, since our LAPW DOS consists of many peaks in the p region which are of comparable size. The same difficulty arises for us to locate a 15.0-eV separation between the oxygen 2s peak and the more tightly bound peak of his valence-band doublet. We can only give a lower and an upper limit of 11 and 17 eV, respectively, for this transition by taking the distance between the LAPW s peak and the beginning and end of the p bands.

A comparison of our full-potential LAPW results with the pseudopotential (PP) calculations of Glassfort et al.[16] shows good correspondence between both ab initio band structures. The s and p bandwidths (1.8 and 5.7 eV) agree exactly, while the separation

(27) Kowalczyk, S. P.; McFeely, F. R.; Ley, L.; Gritsyna, V. T.; Shirley, D. A. *Solid State Commun.* **1977**, *23*, 161.

of the s band center from the Fermi energy (LAPW 17.3, PP 17.0 eV) and the conduction bandwidths (LAPW t_{2g}/e_g 2.6/2.9, PP t_{2g}/e_g 2.9/3.3 eV) differ only slightly. Both calculations underestimate the experimental band gap of 3.0 eV[28,29] considerably (LAPW 1.5, PP 2.0 eV), an effect which is induced by the local-density approximation. In LDA calculations the Kohn–Sham eigenvalues (band energies) rigorously do not represent excitation energies. Furthermore, there is a fundamental difference between occupied and unoccupied states, which are treated the same in LDA but correspond to an N versus $N - 1$ electron system. If one insists on using the LDA energies to estimate the gap, it is well-known that this procedure often leads to only about half the experimental gap.[30] Burdett[13] and earlier Grunes[31] et al. have shown that extended Hückel calculations, which are not based on the LDA, can predict the energy gap of TiO_2 to be 2.8 eV.

The discrepancy between LAPW and pseudopotential results is probably caused by different exchange-correlation potentials (LAPW Hedin–Lundqvist,[32] PP Ceperly–Alder[33]) and by the minimal $\vec{k}$ point set used in the pseudopotential calculation (*one* special point). The LAPW band gap is a direct one and occurs at Γ; an indirect gap, however, between Γ and M is larger by about only 0.14 eV. The energy difference between these two gap types is near the accuracy of a method based on the local-density approximation, so we cannot reliably predict a direct gap. Glassford et al.[16] have reported similar findings and concluded that the present theory cannot interfere with the discussion regardless of whether TiO_2 exhibits a direct or indirect band gap.

6.2. CrO_2. One of the few experimental data available for CrO_2 are XPS measurements by Kämper et al.[34] on polycrystalline CrO_2 films. These measurements are of special interest to us, since the photoelectrons were detected to be spin-resolved. The CrO_2 films were gently cleaned by soft sputtering with a defocused 500-eV Ne ion beam. These authors found extremely low spectral intensities from the Fermi energy down to about 2 eV, where they observed 100% spin polarization and the onset of a peak centered around 2.7 eV below E_F. The shape of this spectrum does not agree with our LAPW DOS. Although we also find 100% spin polarization in our DOS (Figure 7), it starts at −0.9 eV and extends to the Fermi energy. The experimental observation that the 100% spin polarization starts 2 eV below E_F is in contrast to the LAPW DOS. At about 2.0 eV below our Fermi energy, the anionic p-band region is situated where no spin polarization is to be expected, because magnetism normally originates from the transition-metal d electrons. In spite of this discrepancy with experiment, we do not conclude that the band picture must have failed in the case of CrO_2 and stress again that the spectrum involves excitations which can only be estimated from ground-state calculations such as our LAPW results. Furthermore, the low intensities at the Fermi energy in the spectra of Kämper et al. are in contradiction not only to our band structure but also to the metallic conductivity of CrO_2. Further XPS experiments would be desirable to clarify this point.

Chase[35] and Dissanayake[36] carried out polarized reflectivity and thermoreflectance measurements on oriented films of CrO_2. They assigned the structures observed in the spectra to interband transitions on the assumption that the energy separation between the spin-up and spin-down t_{2g} bands will decrease with increasing temperature. They argued that the d bands are split by the ferromagnetic exchange interaction, which will break down at 392 K due to the ferromagnetic–paramagnetic phase transition of CrO_2. They found energy separations between the p bands and the Fermi energy of 1.5 and 1.8 eV from the static reflectivity measurements[35] and thermomodulated spectra,[36] respectively. If we use for these excitations again the LAPW DOS of Figure 7, we can estimate from the upper edge of the p bands a lower energy limit of 0.9 eV for this transition. The splitting between the spin-up and spin-down d subbands amounts to 0.8 eV according to Dissanayake. The much higher LAPW value of 1.6 eV for the exchange splitting at $T = 0$ K is reasonable, since in the spectra (recorded at room temperature) lower spin ordering is to be expected. The transition between the occupied oxygen p bands and the empty Cr spin-down subbands is experimentally[36] found to be in the range between 2.7 and 3.1 eV, depending on the polarization direction of the incident light beam. One obtains a value of about 2.6 eV from the LAPW DOS by taking the separation of the upper p edge from the center of the spin-down t_{2g} peak. Thus, the agreement between these optical spectra and our LAPW band structure is fairly good.

6.3. RuO_2. The electronic structure of RuO_2 has been investigated by Daniels et al.[37] by means of XPS using synchrotron radiation. From the spectra taken at photon energies of 70, 90, 110, and 130 eV, they deduced the existence of four peaks with averaged energies of −1.2, −3.8, −5.8, and −7.35 eV, labeled A, B′, B, and C. The shape of the spectra resembles clearly our calculated DOS. Feature A corresponds unambiguously to the DOS peak at 0.9 eV below E_F which originates from the Ru t_{2g} states. The other features B′–C lie in the range of the oxygen p states (1.7–8.3 eV below E_F). An assignment to specific DOS peaks, however, is difficult to make, since matrix element effects would enhance the metal d cross section over that of oxygen p. The most prominent oxygen peak within the p DOS is situated at 7.2 eV and corresponds most likely to spectral feature C at −7.35 eV.

A comparison of our LAPW DOS with the results of ab initio calculations of Schwarz[38] (by the augmented spherical wave method) and Xu[15] shows nearly quantitative agreement. Xu et al. determined their DOS by means of the self-consistent linear muffin-tin-orbital (LMTO) method. By taking matrix element effects into account, they calculated a theoretical XPS spectrum from their LMTO DOS and found good agreement with the experimental data of Daniels et al. Their largest discrepancy occurs for the position of the low-energy peak which is predicted to be about 0.6 eV closer to E_F.

6.4. ZnF_2. Zinc(II) fluoride has been investigated in an XPS study of Kowalczyk et al.[39] and in two UPS studies of Pong et al.[40] and Poole et al.[41] The agreement between the latter UPS measurements and our LAPW DOS is very satisfying. Poole et al. recorded the spectra with a photon source of 40.81 eV and an instrumental resolution of 0.3 eV. They found an experimental valence bandwidth of 6.2 eV, whereas the corresponding LAPW bandwidth is 6.0 eV. Their photoelectron spectrum shows a clear doublet structure with a peak separation of 3.3 eV. These peaks are identified by Poole et al. to originate from the Zn 3d and the F 2p states, where the latter were situated at the lower binding energy. The same assignment results from the LAPW DOS which shows a Zn t_{2g} peak at −3.3 eV and a F $2p_y$ peak at −1.2 eV. Although the doublet structure is maintained in the other UPS and the XPS measurements, these spectra exhibit features not observed by Pool et al. The XPS spectrum of Kowalczyk et al. shows a very diffuse low-energy peak (labeled e_g), while in the UPS spectrum of Pong et al. the same peak exhibits a noticeable shoulder on the low-energy side. Kowalczyk et al. identified this peak as a satellite due to crystal field splitting in the final d^9 state of ZnF_2. Pong et al. concluded that the crystal field splitting was

(28) Pascual, J.; Camassel, J.; Mathieu, H. *Phys. Rev.* **1978**, *B18*, 5606.
(29) Vos, K.; Krusemeyer, H. J. *J. Phys.* **1977**, *C10*, 3893.
(30) The band gap problem was first pointed out by: Trickey, S. B.; Green, F. R.; Averill, F. W. *Phys. Rev.* **1973**, *B8*, 4822. A summary of the history and references are found in: Perdew, J. *Int. J. Quantum Chem.* **1987**, *S19*, 497.
(31) Grunes, L. A.; Leapman, R. D.; Wilker, C. N.; Hoffmann, R.; Kunz, A. B. *Phys. Rev.* **1982**, *B25*, 7157.
(32) Hedin, L.; Lundqvist, B. I. *J. Phys.* **1971**, *C4*, 2064.
(33) Ceperley, D. M.; Alder, B. J. *Phys. Rev. Lett.* **1980**, *45*, 566.
(34) Kämper, K. P.; Schmitt, W.; Günterodt, G. *Phys. Rev. Lett.* **1987**, *59*, 2788.
(35) Chase, L. L. *Phys. Rev.* **1974**, *B10*, 2226.
(36) Dissanayake, M. A. K. L.; Chase, L. L. *Phys. Rev.* **1981**, *B23*, 6254.
(37) Daniels, R. R.; Margaritondo, G. *Phys. Rev.* **1984**, *B29*, 1813.
(38) Schwarz, K. *Phys. Chem. Miner.* **1987**, *14*, 315.
(39) Kowalczyk, S. P.; Ley, L.; McFeely, F. R.; Pollak, R. A.; Shirley, D. A. *Phys. Rev.* **1974**, *B9*, 381.
(40) Pong, W.; Okada, S. K. *Phys. Rev.* **1979**, *B19*, 5307.
(41) Poole, R. T.; Nicholson, J. A.; Liesegang, J.; Jenkin, J. G.; Leckey, R. C. G. *Phys. Rev.* **1979**, *B20*, 1733.

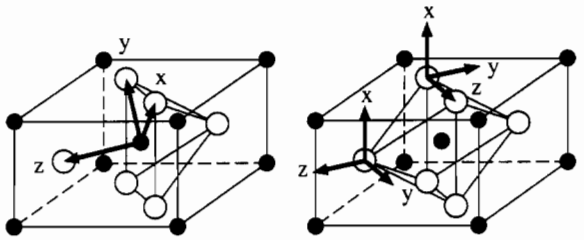

Figure 13. Coordinate systems used inside the atomic spheres: (a) metal position ($^1/_2$, $^1/_2$, $^1/_2$); (b) anion positions (u, u, 0) and ($^1/_2 + u$, $^1/_2 - u$, $^1/_2$). Since these systems are specific for each position, they are called "local systems" throughout text.

Table IV. Muffin-Tin Radii R_{MT} of the Atomic Spheres

atomic sphere	R_{MT}, au	atomic sphere	R_{MT}, au
Ti in TiO_2	1.810	Ru in RuO_2	1.830
O in TiO_2	1.810	O in RuO_2	1.830
V in VO_2	1.780	Zn in ZnF_2	1.8704
O in VO_2	1.780	F in ZnF_2	1.8704
Cr in CrO_2	1.7946		
O in CrO_2	1.7946		

responsible for the occurrence of the peak shoulder in their UPS spectrum. We do not accept this "crystal field splitting" effect for two reasons: first, concerning the XPS study of Kowalczyk et al., we want to remark that satellite peaks do not fall on the low-energy side of the main peak; second, according to an argument of Poole et al., a crystal field splitting of the final state should give peak intensities approximately invariant to changes in photon energy, which is clearly not observed.

Acknowledgment. This project was supported by the Fonds zur Förderung der wissenschaftlichen Forschung, Project No. P5939C. We are most grateful to Elisabeth Sorantin, M.A., for her editorial advice.

Appendix

All calculations were carried out by the Wien LAPW code which is obtainable from the CPC Program Library.[21] The typical input parameters used in these calculations will be given here.

The number of plane waves in the basis set is determined to meet the empirical convergence criterion that $R_{MT}|\vec{k} + \vec{K}_{max}|$ should be at least 8 (R_{MT} is the radius of an atomic sphere, $\vec{k}$ is a given Brillouin-zone vector, and $\vec{K}_{max}$ is the largest reciprocal wavevector used within the basis set). The resulting number of plane waves is about 600. The convergence achieved in the eigenvalues is better than 0.1 mRy.

Inside the atomic spheres, the wave function is expanded in spherical harmonics Y_{lm} up to $l = 12$. The Y_{LM} basis set of electron density and potential is truncated after $L = 4$. The number of Y_{LM} combinations included is minimized[42] by choosing coordinate systems consistent with the point group symmetry of that atomic site. Since these coordinate systems are specific for each atom but differ from the crystal axes, we call them "local" systems. Figure 13 shows the local coordinate systems of the atomic sites (0, 0, 0) and (u, u, 0) which correspond to the metal and anion positions in the rutile structure. The local titanium system in Figure 13 is oriented according to ligand field theory: all axes point toward the six oxygen ligands; namely, the x and y axes point to the atoms in the octahedral base plane and the z axis points to the apical oxygen atoms. The x and y axes, however, are not *exactly* directed toward the oxygen ligands, because of the rectangular distortion of the octahedral base plane. For the interpretation we use this choice of the axes throughout the text, while the calculations are based on the *mmm* point group symmetry of the titanium position: x axis parallel to [$\bar{1}$10], y axis parallel to [110], z axis parallel to [001]. The local oxygen system shown in Figure 13 is identical with the one used in the calculations.

The radial parts of the wave function, electron density, and potential are represented numerically on a logarithmic radial mesh: $\ln r_i = \ln r_0 + d(i - 1)$ with $i = 1...i_{max}$. The largest values (for $i = i_{max}$), the "muffin-tin" radii R_{MT}, are chosen to yield touching atomic spheres. Except for the case of CrO_2, the total number of radii used in the meshes is always 381, the first radius of a mesh ($i = 1$) being 1×10^{-5} au. For CrO_2, i_{max} is 331 and r_0 is 4.654×10^{-5} au. Table IV summarizes the muffin-tin radii for all atoms involved in the calculations. In the interstitial region, electron density and potential are expanded in a Fourier series with about 500 $\vec{K}$ stars. In the energy range of the valence states, the Brillouin-zone integration is based on 24 $\vec{k}$ points, uniformly distributed in the irreducible wedge (IBZ).

The states below the valence bands down to −5 Ry are not sufficiently localized to describe them as core states. We treat these "semicore" states (Ti, V, Cr, Zn (3s, 3p) and Ru (4s, 4p)) with additional band calculations.[21] Since the $\vec{k}$ dispersion of these states is small, a grid of six $\vec{k}$ points in the IBZ is sufficient. The core states are calculated every iteration ("thawed-core approximation") using the spherical part of the potential. Self-consistency is achieved when the total energy of consecutive iterations changes by less than 0.1 mRy.

In all paramagnetic cases the LDA in the parametrization of Hedin–Lundqvist[32] is used, while for ferromagnetic CrO_2 the local spin density approximation with the parameters of Moruzzi–Janak–Williams[43] treats exchange and correlation effects. The density of states is calculated by the tetrahedron method[44] using 24 $\vec{k}$ points except for CrO_2, where we use 60 $\vec{k}$ points in the IBZ.

Registry No. TiO_2, 13463-67-7; VO_2, 12036-21-4; CrO_2, 12018-01-8; RuO_2, 12036-10-1; ZnF_2, 77838-49-4.

(42) Kurki-Suonio, K. *Isr. J. Chem.* **1977**, *16*, 115.
(43) Moruzzi, V. L.; Janak, J. F.; Williams, A. R. *Calculated Electronic Properties of Metals*; Pergamon: New York, 1978.
(44) Lehman, G.; Taut, M. *Phys. Status Solidi B* **1972**, *54*, 469.